# Light-Induced Defect Formation and Pt Single Atoms Synergistically Boost Photocatalytic $H_2$ Production in 2D $TiO_2$-Bronze Nanosheets

Sourav Rej,* S. M. Hossein Hejazi, Zdeněk Badura, Giorgio Zoppellaro, Sergii Kalytchuk, Štěpán Kment, Paolo Fornasiero, and Alberto Naldoni*

**ABSTRACT:** Ultrathin two-dimensional (2D) semiconductor nanosheets decorated with single atomic species (SAs) have recently attracted increasing attention due to their abundant surface-exposed reactive sites and maximum SAs binding capabilities thus lowering the catalyst cost, without sacrificing high performance for photocatalytic hydrogen ($H_2$) production from water. Here, we present a strategy to prepare titanium dioxide-bronze nanosheets ($TiO_2$-BNS) and $H_2$-reduced $TiO_2$ nanosheets ($TiO_2$-HRNS) synthesized, characterized, and applied for photocatalytic $H_2$ production. Surprisingly, black $TiO_2$-HRNS show complete photo inactivity, while the $TiO_2$-BNS-$Pt_{0.05}$ nanohybrid shows excellent $H_2$ production rate with a very low loading of 0.05 wt % Pt. $TiO_2$-BNS-$Pt_{0.05}$ presents around 10 and 99 times higher photocatalytic rate than pristine $TiO_2$-BNS under solar and 365 nm UV-LED light irradiation, respectively. Due to the 2D morphology and the presence of abundant coordinating sites, the successful formation of widely dispersed Pt SAs was achieved. Most excitingly, the *in situ* formation of surface-exposed defect sites ($Ti^{3+}$) was observed for $TiO_2$-BNS under light illumination, suggesting their significant role in enhancing the $H_2$ production rate. This self-activation and amplification behavior of $TiO_2$-BNS can be extended to other 2D systems and applied to other photocatalytic reactions, thus providing a facile approach for fully utilizing noble metal catalysts via the successful formation of SAs.

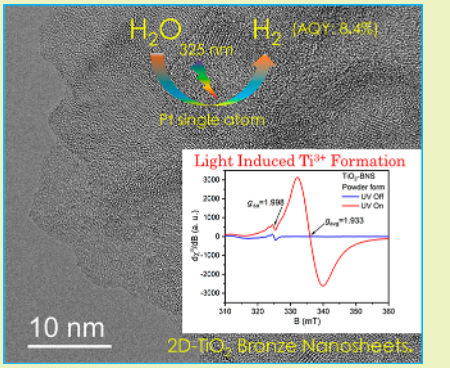


**KEYWORDS:** *$TiO_2$-bronze nanosheets, Hydrogen production, Platinum single atoms, in situ $Ti^{3+}$ formation, Light-induced defect formation*

## INTRODUCTION

Photocatalytic hydrogen production via the water-splitting reaction is considered as an effective way to convert abundant solar energy into chemical energy through the formation of hydrogen, a solar fuel that will be increasingly replacing the use of carbon-based chemicals in the future energy economy.[1−3] Titanium dioxide ($TiO_2$) and the hybrid photocatalysts based on its utilization have been intensively investigated over past decades, which makes it as the benchmark photocatalyst for solar-driven $H_2$ production from water.[4−6] This is due to its excellent chemical stability, environmental benignity, and scarce photocorrosion in photocatalytic conditions. The crystal structure of $TiO_2$ can assume different periodic organizations resulting in the formation of three common polymorphs, namely, anatase (tetragonal), rutile (tetragonal), and brookite (orthorhombic).[7,8] These three crystal phases are the most widely investigated, whereas the bronze phase with the monoclinic crystal structure is less studied for photocatalytic $H_2$ production. Low-dimensional materials such as atomically thick two-dimensional (2D) $TiO_2$-bronze nanosheets ($TiO_2$-BNS) have been recently used in lithium-ion batteries owing to the open channels along the [010] direction, which facilitate the transportation of lithium ions.[9−11] Moreover, 2D nanosheets allow also short-distance diffusions of photoinduced charge carriers, thus promoting the separation of charge carriers and resulting in higher photocatalytic activities.[12,13] In this study, less explored $TiO_2$-BNS were used for green $H_2$ production due to their high surface areas, unique (010) crystal planes, and presence of sufficient reactive sites.

Generally, as $TiO_2$ presents a high recombination rate of photoexcited electron−hole pairs and sluggish kinetics for hydrogen evolution, metal cocatalysts are needed to achieve high catalytic performance.[14,15] Among a wide variety of investigated cocatalysts, Pt offers the best performance, and it is often used as a benchmark reference. Nonetheless, its limited availability and high price make its wide use in large-scale applications more and more difficult. Recently, single atomic species (SAs) of metal cocatalysts have appeared as a new frontier in catalysis because of maximum atom utilization and

the enhanced reactivities of uncoordinated metal ions dispersed on photoactive nanomaterials.[15−17] Downsizing metal nanoparticles to cluster into SAs enhances Pt utilization efficiency without sacrificing the photocatalytic performance. Different ways for decorating Pt SAs onto $TiO_2$ nanocrystals have been developed with higher catalytic efficacies. One of the major challenges to address is that Pt SAs without strong binding sites can be thermodynamically unstable due to their high surface energies and hence tendencies to agglomerate during multiple reaction cycles. For these reasons, a high surface area support with sufficient strong coordination sites is necessary to firmly anchor Pt SAs onto the $TiO_2$ matrix.[18−20]

Herein, using a large-scale green solvothermal synthesis procedure, ultrathin 2D $TiO_2$-BNS were prepared. Both $TiO_2$-BNS and $H_2$-reduced $TiO_2$ nanosheets ($TiO_2$-HRNS) were characterized using different spectroscopic techniques. Surprisingly, $TiO_2$-HRNS show complete photo inactivity due to the formation of graphene-like carbon species on their surfaces during high temperature reduction treatment. Electron paramagnetic resonance (EPR) spectroscopy measurements under photocatalytic conditions revealed that the *in situ* generation of surface-exposed defect sites, i.e., $Ti^{3+}$ on $TiO_2$-BNS, is responsible for the higher photocatalytic $H_2$ production activity. To further enhance performance, we synthesized Pt SA-decorated $TiO_2$-BNS with 0.05 wt % loading ($TiO_2$-BNS-$Pt_{0.05}$), using an easy synthetic procedure. A large surface area with sufficient binding sites, light-induced *in situ* $Ti^{3+}$ defect formation, and very low loading of Pt SAs enhance the photocatalytic $H_2$ production rate of $TiO_2$-BNS-$Pt_{0.05}$ around 10 and 99 times higher than pristine $TiO_2$-BNS under solar and 365 nm UV-LED light irradiation, respectively. These results demonstrate that $TiO_2$-BNS are promising candidates for photocatalytic green hydrogen production from water as well as good matrices for SAs decorations.

## EXPERIMENTAL SECTION

**Synthesis of $TiO_2$-BNS.** $TiO_2$-BNS were synthesized using a reported literature procedure with major modifications adopted to achieve higher yields.[21] Three 45 mL pressure-resistant cylindrical glass vessels were equipped with magnetic stirrers and placed inside large glass beakers. In each of them, 2 mL of $TiCl_3$ aqueous solution (∼15%) was added dropwise into 30 mL of an ethylene glycol solution under stirring at 600 rpm, and it was stirred for 5 min. After that, 2 mL of DI-$H_2O$ was added dropwise in each of the three glass vessels under stirring, followed by stirring for another 5 min. Next, the magnetic stirrers were taken out, and then, each glass vessel was tightly sealed with an O-ring capped lid followed by placing them into a preheated oven at 150 °C for 4 h. Afterward, the glass reactors were taken out from the oven and let to cool to room temperature for 50 min. The precipitate was then washed five times with a DI-$H_2O$/ethanol mixture (1:1 volume ratio) and collected by centrifugation at 13,500 rpm for 5 min and finally dried in a vacuum oven at 60 °C for 12 h. These dried $TiO_2$ powders were crushed into fine powder using a spatula (average isolated yield from three reactors ∼240 mg). The as-obtained white product was labeled as $TiO_2$-BNS.

**Synthesis of $TiO_2$-HRNS.** A ceramic crucible containing 210 mg of $TiO_2$-BNS was placed in a tube furnace. The reduction process was carried out in 10 vol % $H_2$ balanced with $N_2$ at 350 °C for 5 h using a heating rate of 2 °C $min^{-1}$ with a gas flow rate 100 mL $min^{-1}$. The cooling rate was also fixed at 2 °C $min^{-1}$. The obtained product (∼170 mg) turned completely black after the reduction process, which was termed as $TiO_2$-HRNS.

**Synthesis of $TiO_2$-BNS-$Pt_x$ Hybrid Nanostructures.** In a 21 mL test tube, 99 mg of $TiO_2$-BNS, 7 mL of DI-$H_2O$, and 1 mL of ethylene glycol were added in a sequence, followed by sonication for 3 min to make a homogeneous solution and then kept under stirring at 900 rpm. Next, a solution containing 2.12 mg of $K_2PtCl_4$ and 2 mL of a DI-$H_2O$/EG mixture (1:1 volume ratio) was prepared and added dropwise into the $TiO_2$-BNS solution under vigorous stirring at 900 rpm within 40 s from its preparation (This step is very important, see Figure S1 and Scheme S1). Afterward, the test tube containing the reaction mixture was quickly placed in a 55 °C preheated oil bath for 2 h, protected from light by covering with aluminum foil. The obtained precipitate was then washed with the DI-$H_2O$/ethanol mixture (1:1 volume ratio) and separated by centrifugation at 13,500 rpm for 5 min using three cleaning cycles and finally dried in a vacuum oven at 60 °C for 12 h. The dried $TiO_2$ was then crushed into fine powder using a spatula and used as is for photocatalytic reactions. The obtained hybrid photocatalyst was termed as $TiO_2$-BNS-$Pt_1$ ($TiO_2$-BNS-$Pt_x$; where $x$ stands for nominal loading of Pt in wt %). $TiO_2$-BNS-$Pt_{0.5}$ and $TiO_2$-BNS-$Pt_{0.05}$ were also prepared using 99.5 mg and 99.9 mg of $TiO_2$-BNS and 1.06 mg and 0.10 mg of $K_2PtCl_4$, respectively, keeping all the other parameters fixed. The Pt loadings in the three samples were confirmed by means of inductively coupled plasma-mass spectrometry and were 0.92%, 0.47%, and 0.04%, respectively. Furthermore, $TiO_2$-HRNS-$Pt_1$ was also synthesized following the same above-mentioned procedure, but using $TiO_2$-HRNS powder as the support material.

**Characterization.** X-ray diffraction patterns of the materials were determined using an X'Pert PRO MPD diffractometer (PANalytical) with iron-filtered CoK$\alpha$ radiation (40 kV, 30 mA, $\lambda$ = 0.1789 nm). Fourier transform infrared (FT-IR) spectra were obtained on a NikoletTM iS50 FTIR spectrometer. X-ray photoelectron spectroscopy (XPS) analyses were performed on a PHI 5000 VersaProbe II XPS system (Physical Electronics) with a monochromatic Al K$\alpha$ source (15 kV, 50 W) and a photon energy of 1486.7 eV. High-resolution spectra were scaled using the adventitious carbon peak as a reference. Raman spectra were collected using a DXR Raman spectrometer (Thermo Scientific, Massachusetts, USA). The surface area analyses were performed by means of $N_2$ adsorption/desorption measurements at the liquid nitrogen temperature on a volumetric gas adsorption analyzer 3 Flex (Micromeritics, Georgia, USA) up to 0.965 $P/P_0$. The ultraviolet−visible diffuse reflectance spectra (UV−vis DRS) of the samples were obtained by a Specord 250 plus (Analytik Jena, Jena, Germany) spectrophotometer. The low-resolution imaging of catalyst morphology was obtained with a transmission electron microscope (TEM) JEOL, equipped with a $LaB_6$ emission gun and operating at 160 kV. A high-resolution transmission electron microscope (HRTEM, FEI TITAN G2 60-300) was used for obtaining HAADF-STEM micrographs.

*Electron Paramagnetic Resonance Spectroscopy Measurements.* Continuous-wave electron paramagnetic resonance (CW-EPR) and light-induced electron paramagnetic resonance (LEPR) technique spectra were recorded on a JEOL JES-X-320 spectrometer (JEOL, Tokyo, Japan) operating at an X-band frequency (∼9.0−9.1 GHz) equipped with a variable-temperature controller (He, $N_2$) ES-CT470 apparatus. The cavity quality factor (Q) was kept above 6500 in all measurements. Highly pure quartz tubes were employed (Suprasil, Wilmad, ≤0.5 OD), and accuracy on $g$-values was obtained against the Mn(II)/MgO standard (JEOL standard). *In situ* light excitation EPR experiments (LEPR) were performed using a HeCd laser source operating at 325 nm (max output power of 200 mW) from Kimmon Koha Co. Ltd. (Tokyo, Japan). The UV light was shined directly onto the sample, kept frozen inside the cavity EPR resonator, through its dedicated optical window.

*Photoluminescence Spectroscopy Measurements.* The photoluminescence (PL) spectroscopy measurements were performed on a FLS980 fluorescence spectrometer (Edinburgh Instruments) with double monochromators on both excitation and emission sides, equipped with a R928P photomultiplier in a thermoelectrically cooled housing (Hamamatsu Photonics), with a 450 W xenon arc lamp as the excitation source for steady-state measurements. Spectral correction curves were provided by Edinburgh Instruments.

For time-resolved measurements, an EPL-375 ps pulsed diode laser ($\lambda_{em}$ = 372 nm with a pulse width of 66.5 ps, a repetition rate of 20 MHz, and an average power of 75 $\mu$W; Edinburgh Instruments) in

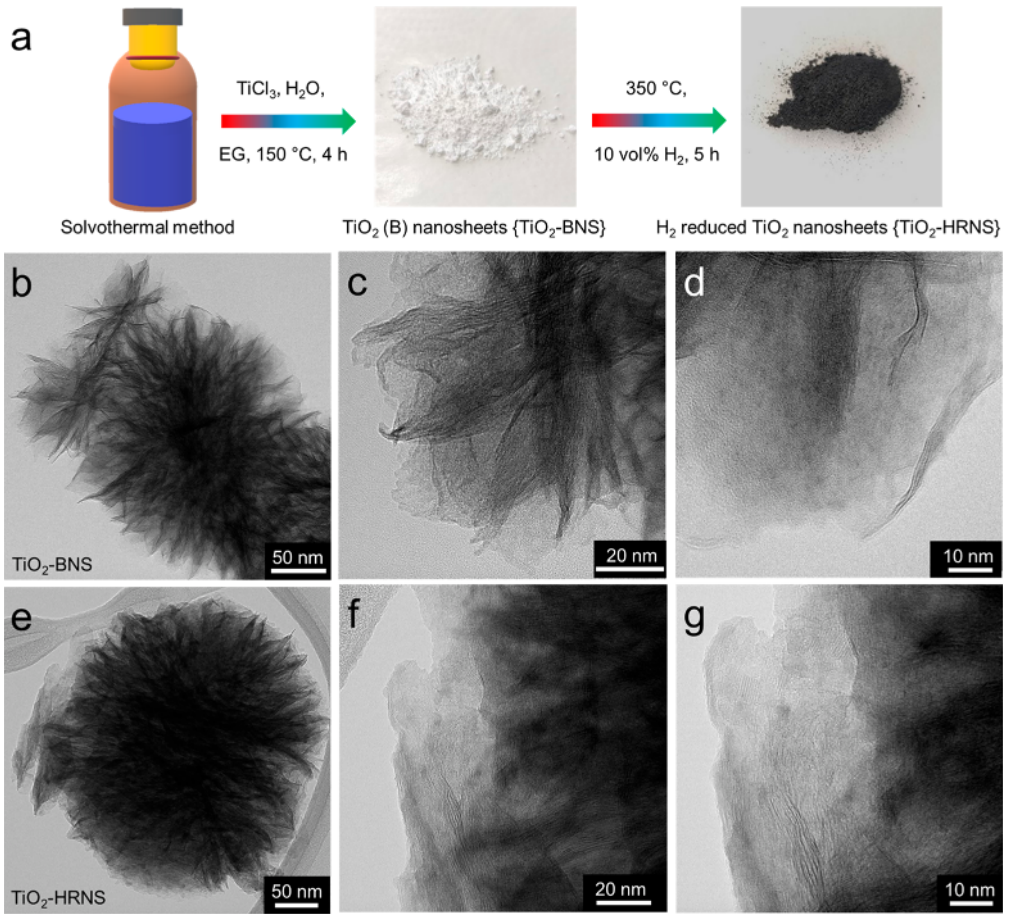


**Figure 1.** Materials synthesis and morphology evaluation: (a) Schematic diagram for syntheses of $TiO_2$-BNS and $TiO_2$-HRNS with corresponding color comparison. TEM images with different magnifications of (b–d) $TiO_2$-BNS and (e–g) $TiO_2$-HRNS, confirming the preservation of nanosheet-like structures even after reduction treatment.

conjunction with a time-correlated single photon counting (TCSPC) system were used. The obtained PL decay curves were fitted using a two-exponential function

$$I(t) = \sum_{i=1}^{2} B_i \exp\left(-\frac{t}{\tau_i}\right), \sum_{i=1}^{2} B_i = 1 \quad (1)$$

in this expression, $\tau_i$ represent the decay time constants, and $B_i$ represent the normalized amplitudes of each component. The amplitude weighted average decay lifetime, $\tau_{avg}$, of the entire fluorescence decay process was calculated in the form

$$\tau_{avg} = \frac{\tau_i B_i}{\sum \tau_i B_i} \quad (2)$$

Powder samples were mounted on a front face sample holder using a dedicated quartz cell holder. Low temperature PL measurements were performed using a variable-temperature liquid nitrogen optical cryostat OptistatDN2 controlled via a cryogenic programmable temperature controller MercuryiTC (Oxford Instruments) with a temperature stability of ±0.1 K (measured over 10 min). Time-resolved PL spectra for different samples were measured with identical instrument settings (identical excitation/emission band-passes and integration times).

**Photocatalytic $H_2$ Evolution Activity Measurements.** In a 33 mL quartz round bottle flask equipped with a magnetic stirrer, an optimized mass of 2 mg of photocatalyst was introduced followed by addition of 11 mL of DI-$H_2O$ and 11 mL of methanol. The reactor was tightly sealed with a rubber septum, then sonicated for 1 min to create a homogeneous suspension. Afterward, the suspension was bubbled with argon (Ar) for 20 min to remove the unwanted gases and dissolved oxygen. The samples were irradiated using a solar simulator equipped with a 150 W Xe arc lamp (AM 1.5G filter) and incident intensity kept fixed at 170 mW $cm^{-2}$ (i.e., 1.7 Sun). The photocatalytic reactions were carried out for 2 h under constant stirring at 900 rpm, and then, the amount of evolved hydrogen was measured using a gas chromatograph GCMS-QP2010 SE (Shimadzu, Kyoto, Japan) equipped with a TCD (thermal conductivity detector), using Ar as the carrier gas. The test was repeated three times, and the average amount of measured hydrogen was reported with error bars.

In addition to solar light, photocatalytic activity was also measured under 365 nm UV-LED light. For these experiments, an optimized mass of about 2 mg of photocatalyst was introduced in a 21 mL quartz test tube equipped with a magnetic stirrer, followed by the addition of 3 mL of DI-$H_2O$ and 3 mL of methanol. The reactor was tightly sealed with a rubber septum, and then, the rest of the steps followed were the same as the above-mentioned steps.

The apparent quantum yield (AQY) was calculated according to the following equation:

$$\text{AQY} = \frac{\text{Number of reacted electrons}}{\text{Number of incident photons}} \times 100 = \frac{2 \times \text{Number of evolved } H_2 \text{ molecules}}{\text{Number of incident photons}} \times 100 \quad (3)$$

## RESULTS AND DISCUSSION

**Morphology and Structural Characterization of Photocatalysts.** The schematic diagram shown in Figure 1a represents the synthesis of $TiO_2$-BNS (white powder) and its

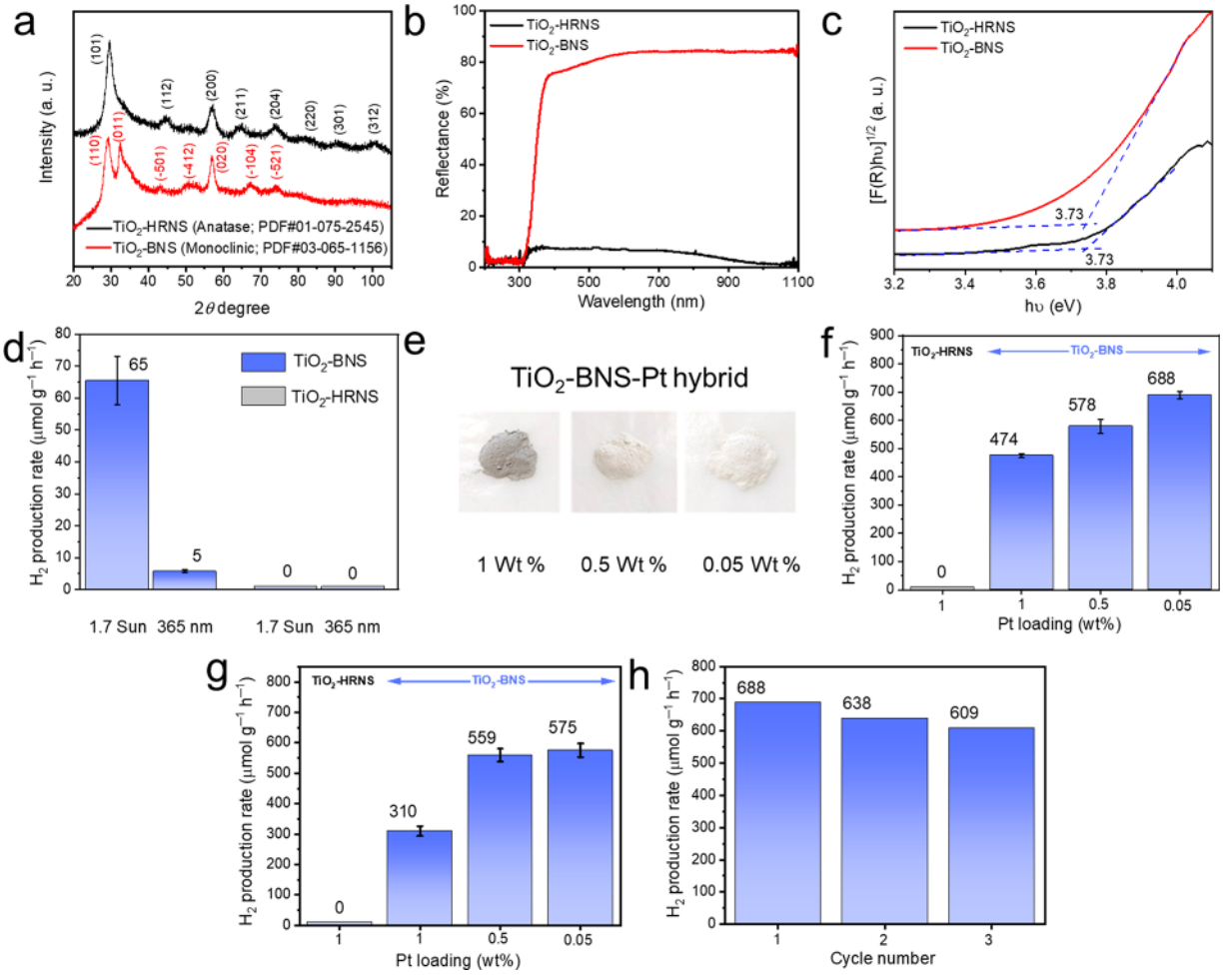


**Figure 2.** Materials characterization and photocatalytic activity comparison: (a) XRD patterns, (b) UV−vis DRS spectra, and (c) corresponding Tauc plots for $TiO_2$-BNS and $TiO_2$-HRNS. (d) Comparison of photocatalytic $H_2$ evolution activities of pure $TiO_2$-BNS and $TiO_2$-HRNS. (e) Digital color pictures of $TiO_2$-BNS hybrid photocatalysts with three different Pt loadings. Photocatalytic $H_2$ evolution activity measurements of the synthesized hybrid photocatalysts under (f) 1.7 sun and (g) 365 nm LED light irradiation. (h) Recyclability test of $TiO_2$-BNS-$Pt_{0.05}$ under 1.7 sun.

subsequent pseudomorphic conversion into $TiO_2$-HRNS (black powder) using a simple $H_2$ reduction method. $TiO_2$-BNS were synthesized by hydrolyzing $TiCl_3$ in ethylene glycol (EG) solvent at 150 °C for 4 h. EG stabilizes efficiently the $TiO_2$-bronze phase during the solvothermal process, thus favoring the formation of this unusual crystal phase.[22] $TiO_2$-BNS were then reduced at 350 °C for 5 h under continuous $H_2$ flow to introduce defects while preserving the nanosheets morphologies. Transmission electron microscopy (TEM) confirms the folded ultrathin 2D nanosheet morphologies both in $TiO_2$-BNS (Figure 1b−d) and $TiO_2$-HRNS (Figure 1e−g) using three different magnifications. Furthermore, high-resolution transmission electron microscopy (HRTEM) of $TiO_2$-BNS confirms its atomically thin 2D nanosheet-like structure with a typical polycrystalline structure with crisscross lattice fringes (Figure S2).[23] The $N_2$ adsorption/desorption isotherms are shown in Figure S3 for $TiO_2$-BNS, from which a specific surface area of 304 $m^2\ g^{-1}$ was retrieved. Such a high surface area ensures widely dispersed anchoring sites for active cocatalysts, adsorption of reactant molecules, and a large number of reactive sites, thus benefiting for enhanced photocatalytic activity.[12,24]

The XRD patterns of $TiO_2$-BNS and $TiO_2$-HRNS are shown in Figure 2a. The XRD patterns of the synthesized $TiO_2$-BNS correspond to the standard monoclinic crystal system of bronze $TiO_2$ [PDF card No. 03-065-1156; Space Group: P21/m (11)]. After $H_2$ reduction, the as-obtained $TiO_2$-HRNS show the standard tetragonal crystal system of anatase $TiO_2$ [PDF card No. 01-075-2545; Space Group: I41/amd (141)], confirming the successful pseudomorphic conversion of bronze nanosheets into anatase nanosheets under the described reduction conditions. Figure 2b shows the UV−vis diffuse-reflectance spectra (UV−vis DRS) of the pristine $TiO_2$-BNS and $TiO_2$-HRNS. The band-edge absorption lies for both samples in the UV region at wavelength < 326 nm. The light absorption of $TiO_2$-HRNS is drastically enhanced from ∼326 nm up to the near-infrared region at ∼1100 nm. Such strong light absorption capabilities of $TiO_2$-HRNS make them suitable candidates for enhanced photocatalytic performances as compared to $TiO_2$-BNS, for which light absorption is mainly limited into the UV region. The band gap values of $TiO_2$-BNS and $TiO_2$-HRNS retrieved from the Tauc plots are shown in Figure 2c, indicating a band gap energy of 3.73 eV for both the samples. It is surprising to notice that, although they possess hugely different light absorbing properties, there is no change in band gap even after the reduction process at high temperature. Notably, $TiO_2$-BNS show higher band gap energies of 3.73 eV, as compared to common $TiO_2$ (∼3.2−

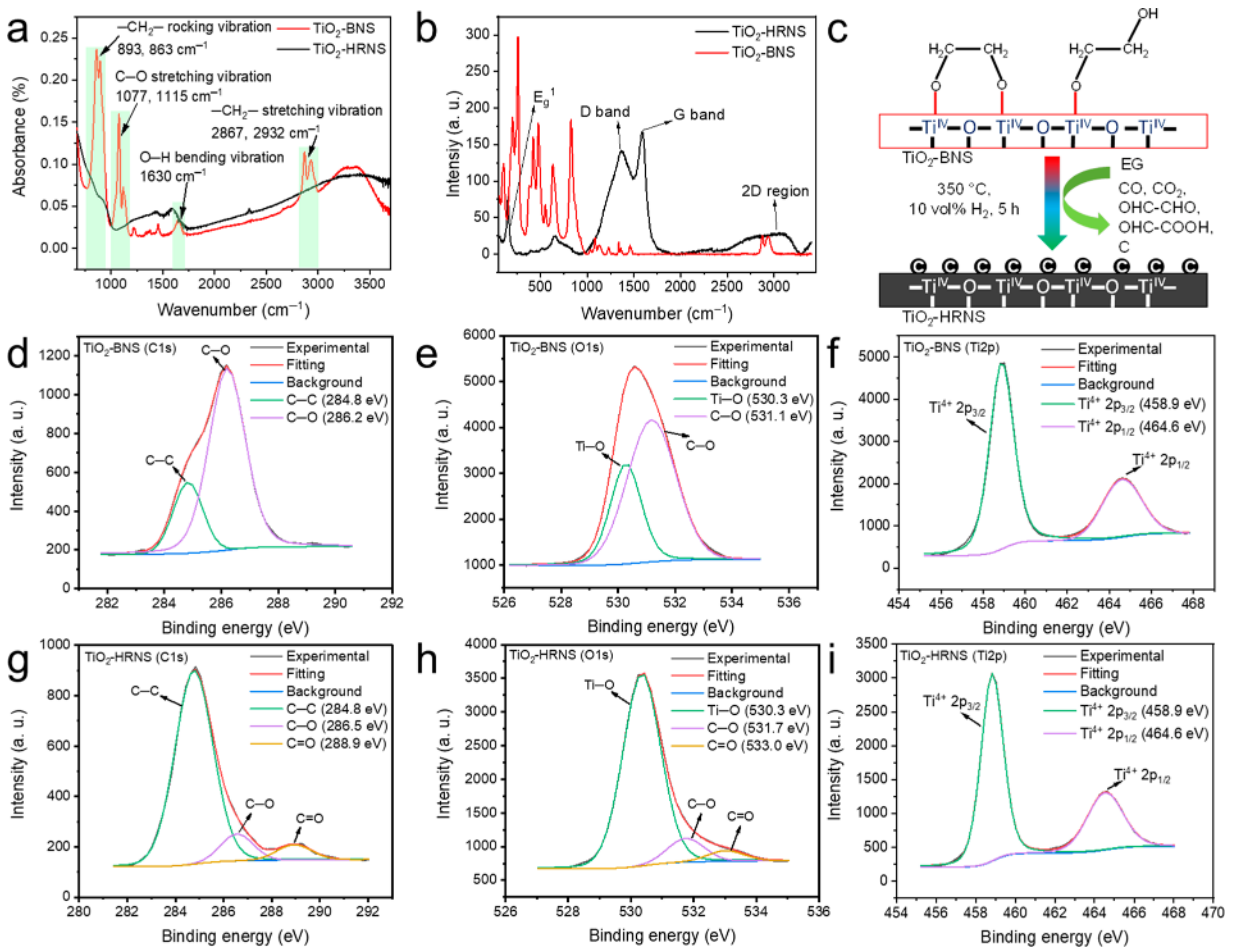


**Figure 3.** Surface composition of photocatalysts: (a) FTIR spectra, (b) Raman spectra, and (c) schematic diagrams for the changes of surface composition for $TiO_2$-BNS and $TiO_2$-HRNS. HRXPS of $TiO_2$-BNS in the (d) C 1s, (e) O 1s, and (f) Ti 2p regions. HRXPS of $TiO_2$-HRNS in the (g) C 1s, (h) O 1s, and (i) Ti 2p regions.

3.3 eV) polymorphs.[25] Wang et al. nicely proved that band gap energies of $TiO_2$-bronze nanosheets vary with ethylene glycol surface coverage ($\theta$).[26] The band gap varied from 3.19 eV at $\theta < 0.56$ to 3.58 eV at $\theta = 1.00$. At very high coverages ($\theta \geq 1$), strong bonding between oxygen atoms of the ethylene glycol molecule and the $Ti^{4+}$ surface atoms effectively control the electronic structures and optical properties of the nanosheets. Therefore, 3.73 eV band gaps for $TiO_2$-BNS suggest higher surface coverages of ethylene glycol molecules onto the nanosheet surfaces.

**Catalytic Performance Evaluation.** Photocatalytic $H_2$ generation performances for both $TiO_2$-BNS and $TiO_2$-HRNS were evaluated using solar irradiation with 1.7 sun intensity. As shown in Figure 2d, $TiO_2$-BNS displays a $H_2$ production rate of 65.5 $\mu$mol g$^{-1}$ h$^{-1}$, whereas $TiO_2$-HRNS surprisingly shows no $H_2$ production even after a high temperature $H_2$ reduction process. Such a finding is uncommon as compared to previous literature reports where after reduction of $TiO_2$ nanocrystals the introduction of defective sites such as $Ti^{3+}$ and oxygen vacancies in the crystal lattice increased the photocatalytic $H_2$ production as compared to pristine samples.[6,27,28] Under 365 nm UV-LED light, the 5.8 $\mu$mol g$^{-1}$ h$^{-1}$ $H_2$ production rate was observed for $TiO_2$-BNS, whereas $TiO_2$-HRNS again did not show any $H_2$ production activity. Such a finding confirms that even though black $TiO_2$-HRNS absorb solar light more efficiently than $TiO_2$-BNS, the photogenerated electron–hole pairs are not useable for $H_2$ production. Photogenerated electrons and holes are not able either to reduce $H^+$ to $H_2$ or oxidize MeOH molecules to subsequent oxidized products, respectively, thus they recombine at the end without producing any detectable $H_2$ gas molecules.

Next, nominal 1, 0.5, and 0.05 wt % Pt were loaded on prepared $TiO_2$-BNS using the ethylene glycol reduction method. Figure 2e confirms the formation $TiO_2$-BNS-Pt$_x$ hybrids by comparing their clear change in color. $TiO_2$-BNS-Pt$_1$ appears gray in color, whereas $TiO_2$-BNS-Pt$_{0.05}$ appears white as the pristine sample. Figure 2f and g shows that with decreasing Pt loading from 1 to 0.05 wt %, the photocatalytic $H_2$ production rate increased under both kinds of light irradiation. $TiO_2$-BNS-Pt$_{0.05}$ showed around 10 and 99 times higher photocatalytic $H_2$ production rates in comparison to pristine $TiO_2$-BNS under solar and 365 nm UV-LED light irradiation, respectively. The highest $H_2$ production rate obtained from $TiO_2$-BNS-Pt$_{0.05}$ is around 688.7 and 575.6 $\mu$mol g$^{-1}$ h$^{-1}$ under solar and UV light irradiation, respectively. Under 365 nm UV-LED light irradiation, an AQY of 2.9% was obtained for $TiO_2$-BNS-Pt$_{0.05}$. With further decreasing the Pt loading, photocatalytic $H_2$ production activity decreased to 120 $\mu$mol g$^{-1}$ h$^{-1}$ under solar irradiation for $TiO_2$-BNS-Pt$_{0.02}$. Table S1 provides a comparison of photocatalytic $H_2$ production rates of different hybrid systems based on $TiO_2$-

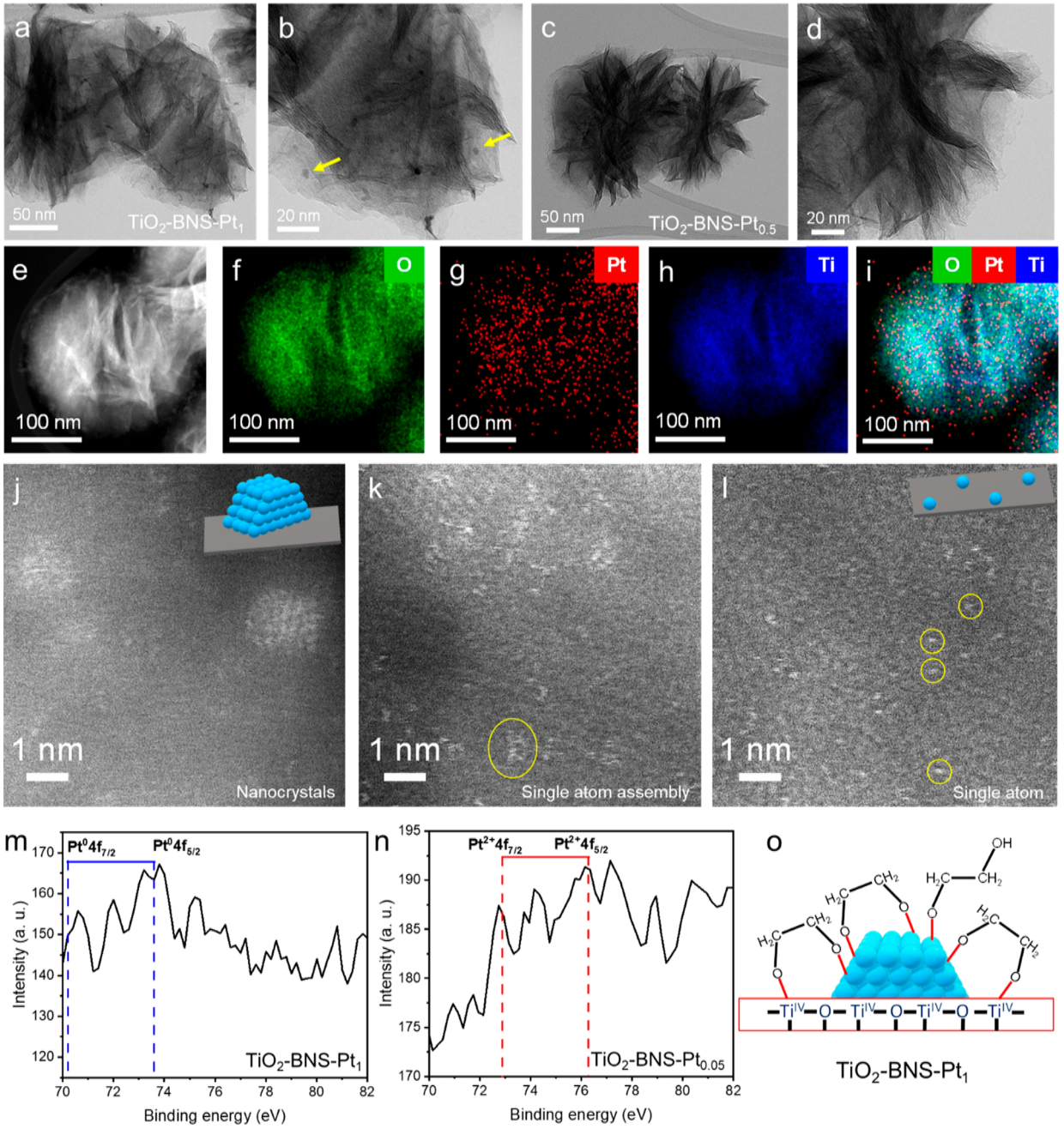


**Figure 4.** Characterization of $TiO_2$-BNS-$Pt_x$: TEM images of (a, b) $TiO_2$-BNS-$Pt_1$ and (c, d) $TiO_2$-BNS-$Pt_{0.5}$ with different magnifications. (e) HAADF-STEM image of $TiO_2$-BNS-$Pt_1$ and (f–i) corresponding EDS elemental maps of $TiO_2$-BNS-$Pt_1$. HAADF-STEM images of (j) $TiO_2$-BNS-$Pt_1$, (k) $TiO_2$-BNS-$Pt_{0.5}$, and (l) $TiO_2$-BNS-$Pt_{0.05}$. Inset shows schematic diagram depicting the form of Pt species present in different samples. HRXPS of Pt 4f region for (m) $TiO_2$-BNS-$Pt_1$ and (n) $TiO_2$-BNS-$Pt_{0.05}$ samples. (o) Pictorial diagram shows high surface coverage on Pt nanocrystals with ethylene glycol molecules in $TiO_2$-BNS-$Pt_1$.

bronze nanomaterials. Using the same synthetic procedure, $TiO_2$-HRNS-$Pt_1$ was prepared, and still no photocatalytic $H_2$ production was observed (Figure 2f and g), even after Pt loading. $TiO_2$-BNS-$Pt_{0.05}$ exhibits reproducible photocatalytic activity in the three consecutive cycling tests (Figure 2h), along with preserving structural and morphological stabilities (Figure S4). Furthermore, when illuminated with 325 nm UV-LED (intensity: 43 mW $cm^{-2}$), $TiO_2$-BNS-$Pt_{0.05}$ showed a 7 mmol $g^{-1}$ $h^{-1}$ $H_2$ production rate with an AQY value of 8.48%.

**In-Depth Surface Composition Analysis.** To understand the photo inactivity of $TiO_2$-HRNS, an advanced surface composition characterization was carried out. Figure 3a shows the FTIR spectra of $TiO_2$-BNS and $TiO_2$-HRNS. In the case of $TiO_2$-BNS, all the stretching, bending, and rocking vibration peaks related to the functional groups (such as $-CH_2-$, C–O, O–H) present in the ethylene glycol molecule are found, which confirm the strong binding interactions of EG molecules with $TiO_2$-bronze nanosheets.[29,30] Surprisingly, all the peaks related to EG molecules were completely absent in the FTIR spectrum of $TiO_2$-HRNS. To understand better this finding, Raman scattering spectroscopy was carried out (Figure 3b) for $TiO_2$-BNS and $TiO_2$-HRNS.[31] The Raman spectrum of $TiO_2$-BNS is consistent with the spectrum of the $TiO_2$-bronze phase. On the other hand, the presence of the scattering peak at 142

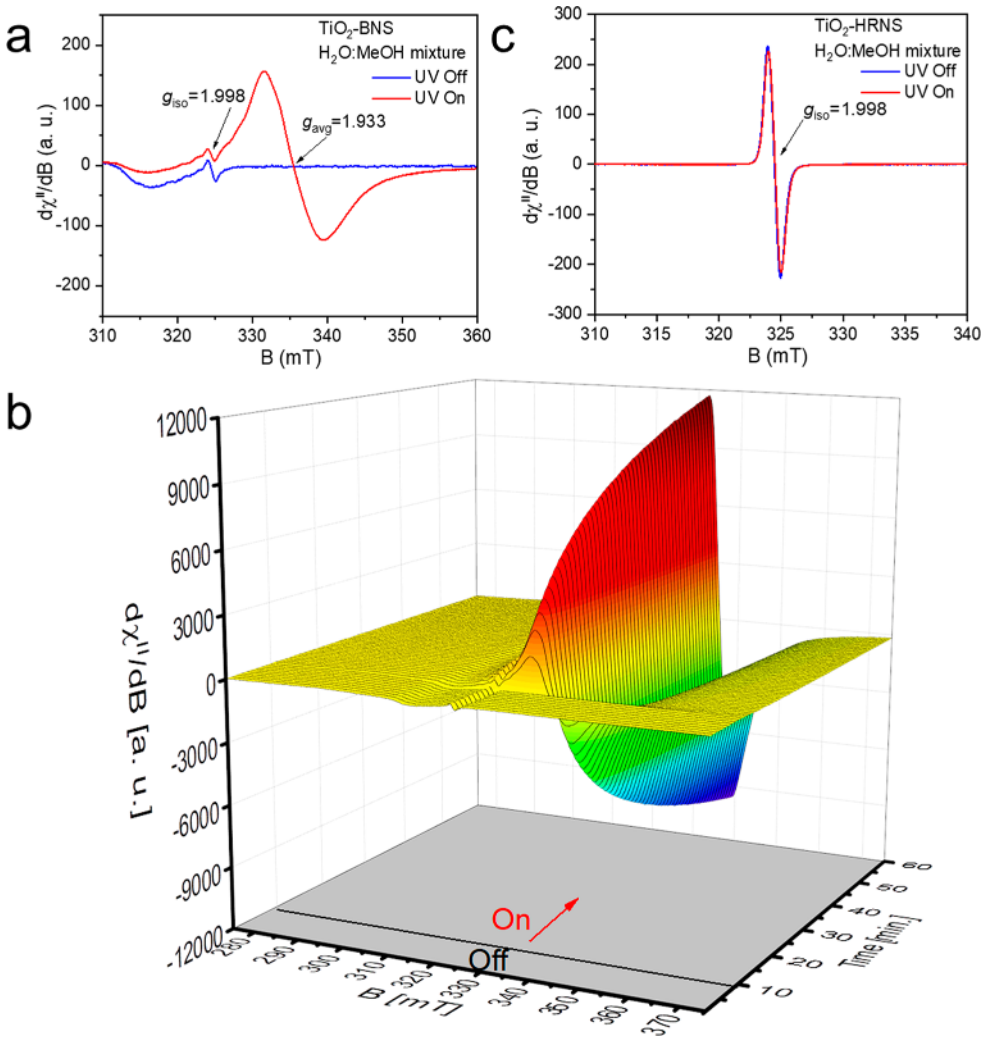


**Figure 5.** Evaluation of EPR spectra: (a) CW X-band EPR spectra of pure $TiO_2$-BNS under dark and 325 nm UV light irradiation in a $H_2O$:MeOH mixture (1:1 volume ratio). (b) Time-dependent 3D spectra plot obtained from *in situ* CW-LEPR measurements using pure $TiO_2$-BNS. (c) CW X-band EPR spectra of $TiO_2$-HRNS under dark and 325 nm UV light irradiation in a $H_2O$:MeOH mixture (1:1 volume ratio).

$cm^{-1}$ (characteristic $E_g^1$ mode of anatase) in $TiO_2$-HRNS confirms its anatase crystal phase. Notably, the presences of the strongest scattering peaks at 1352 $cm^{-1}$ (D band), 1588 $cm^{-1}$ (G band), and 2400−3250 $cm^{-1}$ (2D region) confirm the presence of graphene nanosheets onto $TiO_2$-HRNS surfaces which form after the high temperature $H_2$ reduction procedure, as shown in the schematic diagram reported in Figure 3c.[32,33]

To further confirm such observations, XPS characterizations were carried out for both samples to understand the chemical surface compositions (Figure S5, Figure 3d−i). HRXPS of C 1s and O 1s regions for $TiO_2$-BNS clearly suggest the presence of EG on the $TiO_2$-bronze nanosheet surface as there is a prominent peak arising from the C−O bond. In contrast, the HRXPS C 1s and O 1s spectra for $TiO_2$-HRNS revealed the absence of the C−O bond with an increasing peak intensity for the C−C bond and Ti−O bond, respectively. Such observations confirmed that the thermal decomposition of surface-bound EG molecules into carbon residues occurred in $TiO_2$-HRNS. Both the samples showed the typical deconvoluted peaks for the $Ti^{4+}$ oxidation state (Figure 3f, i) in $TiO_2$. The absence of $Ti^{3+}$ peaks in $TiO_2$-HRNS suggests that the high temperature $H_2$ reduction induces mainly two effects: (i) the decomposition of EG molecules into surface-attached graphene species and (ii) the pseudomorphic bronze to anatase phase transition. It can be concluded that the presence of graphene-like carbon on the surfaces of $TiO_2$-HRNS acts as a catalyst poison, i.e., photogenerated electron−hole recombination center, making them not useful for reduction of $H^+$ to $H_2$.

**Identification of Pt SAs.** With decreasing Pt loading from 1 to 0.05 wt % on $TiO_2$-BNS, the photocatalytic $H_2$ production rate was remarkably enhanced under both solar and UV light irradiation. Such an interesting finding suggested the formation of Pt SAs at 0.05 wt % loading with maximum atom utilization (Pt loading decreased by 20 times). Figure 4a and b shows TEM images of $TiO_2$-BNS-$Pt_1$ under two different magnifications, which confirm that it contains well-dispersed Pt nanocrystals with an average size of 1.8 ± 0.2 nm (marked by yellow arrows in Figure 4b). In contrast, no formation of Pt nanocrystals was observed in $TiO_2$-BNS-$Pt_{0.5}$ (Figure 4c and d) suggesting that Pt may be in the form of single atomic species. The HAADF-STEM image for $TiO_2$-BNS-$Pt_1$ (Figure 4e) and its corresponding elemental mappings for oxygen, platinum, titanium, and their overlap (Figure 4f−i) further confirmed the presence of Pt nanocrystals in the sample. For more in-depth observation, the HAADF-STEM images of

$TiO_2$-BNS-$Pt_1$ (Figure 4j), $TiO_2$-BNS-$Pt_{0.5}$ (Figure 4k), and $TiO_2$-BNS-$Pt_{0.05}$ (Figure 4l) confirm that Pt is present as nanoparticles, single atom assemblies, and well-separated single atomic species, respectively. This observation strongly suggests that a high concentration of $K_2PtCl_4$ results in faster reduction in the presence of ethylene glycol (EG), which leads to the formation of EG-stabilized Pt nanocrystals, whereas lower concentration (0.05 wt %) leads to a slower reduction rate and no aggregation of Pt atoms; i.e., each Pt atom is well separated and strongly coordinated by EG molecules onto the $TiO_2$-BNS surfaces (Figure S1 and Scheme 1). Thus, surface-attached EG molecules help to stabilize Pt SAs onto $TiO_2$-BNS surfaces via their strong chelating properties and also prevent them from sintering during photocatalysis.[30]

To understand the oxidation states for Pt species, we performed XPS of $TiO_2$-BNS-$Pt_1$ and $TiO_2$-BNS-$Pt_{0.05}$ (Figure S6). Most surprisingly, from HRXPS of the Pt 4f regions for $TiO_2$-BNS-$Pt_1$ (Figure 4m) and $TiO_2$-BNS-$Pt_{0.05}$ (Figure 4n), no well-defined peak for Pt was observed, instead it looks like a noisy weak peak. Absence of any well-defined Pt peak in both of these samples can be associated with high surface coverage of ethylene glycol molecules on these nanostructures. Thermal calcination of $TiO_2$-BNS-$Pt_1$ at 350 °C for 5 h in a muffle furnace shows around ~19% weight loss which comes from the oxidation of surface organic ligands, and this value is comparable with previous reports (surface coverage of EG ~ 27% in $TiO_2$-BNS).[26] Such high surface coverage of organic EG molecules onto a $TiO_2$-BNS-$Pt_1$ surface (Figure 4o) is hindered from obtaining clear HRXPS signals for the Pt 4f region, even with 1 wt % Pt loading. Chen et al. recently also obtained a noisy weak signal from $TiO_2$-BNS decorated with $MoS_3$ quantum dot cocatalysts even when using 2 wt % loading.[34] Though the HRXPS signals for the Pt 4f regions are weak in both samples, a close inspection may suggest that Pt oxidation states in $TiO_2$-BNS-$Pt_1$ and $TiO_2$-BNS-$Pt_{0.05}$ are 0 and +2, respectively. In Figure 4m, blue lines suggest Pt is in the metallic state with peaks at 70.10 and 73.43 eV corresponding to $Pt^0 4f_{7/2}$ and $Pt^0 4f_{5/2}$, respectively.[18] Similarly, in Figure 4n, red lines suggest that Pt is in the +2 oxidation state with peaks at 72.80 and 76.13 eV corresponding to $Pt^{2+} 4f_{7/2}$ and $Pt^{2+} 4f_{5/2}$, respectively.[35]

***In Situ* Detection of the Photogenerated $Ti^{3+}$ Defect.** To screen the physical effects generated by reduction of $TiO_2$-BNS to $TiO_2$-HRNS and to probe the electronic perturbations and/or redox processes induced by the $TiO_2$ spin containing defects, detailed *in situ* electron paramagnetic resonance (EPR) studies were carried out without and under *in situ* UV light irradiation.

For these measurements, nanopowder slurries were placed in quartz EPR tubes, using $O_2$-free solutions (1:1 volume ratio of $H_2O$: methanol) at a liquid nitrogen temperature. Figure 5a represents the continuous-wave electron paramagnetic resonance (CW-EPR) spectra recorded both in dark and under light conditions for the $TiO_2$-BNS.[36−39] Under the dark condition (Figure 5a, blue line), a weak resonant signal appears at $g$ = 1.998, which can be assigned to $S$ = 1/2 centers localized onto Ti sites ($Ti^{3+}$) positioned in the lattice of the $TiO_2$ nanosheets.[39,40] This weak signal is not influenced by illumination. Under light illumination, a significantly strong but broad signal appears at $g_{avg}$ = 1.933, which corresponds to the formation of a substantial number of surface-exposed $Ti^{3+}$ centers.[36−39] This observation can be explained by the photoreduction of a significant amount of $Ti^{4+}$ to $Ti^{3+}$ species through the photoexcited electrons, also known as light-induced defect formation. Such a clear increase in $Ti^{3+}$ surface-exposed sites with respect to time, upon UV irradiation, can be seen in the 3D *in situ* continuous-wave light-induced electron paramagnetic resonance (CW-LEPR) contour plot (Figure 5b). The development of such a strong resonance signal with time demonstrates that when the UV light is provided to the sample, *in situ* generated $Ti^{3+}$ defect sites capable to promote $H_2$ generation are formed (Figure 2d). Reduced $TiO_2$-HRNS does not exhibit any photocatalytic water-splitting efficiency. The EPR spectrum of $TiO_2$-HRNS under dark conditions (Figure 5c, blue line) is characterized by a sharp isotropic signal at $g_{iso}$ = 1.998 with line width of 0.6 mT. This strong peak, with its isotropic features, can be associated with C-based radical centers arising from the presence of excess graphene-like carbon residue on the surfaces of $TiO_2$-HRNS, in agreement with the materials' Raman and HRXPS analyses (Figure 3b, g).[41] No substantial change was observed in the recorded EPR spectra under UV light irradiation (Figure 5c, red line), thus confirming that the $TiO_2$-HRNS material does not generate long living new spin centers during UV photoexcitation, and the electron−hole recombination processes become here extremely efficient which underlies the photo inactivity of the sample. Both the samples even in powder form, under dark and UV-irradiation conditions, show similar characteristic EPR peaks as those observed in a frozen $H_2O$/MeOH solvent mixture (Figure S7). Such exciting phenomenon shows a new pathway on which, shining light particularly on $TiO_2$-BNS, induces the *in situ* formation of desired surface-exposed $Ti^{3+}$ defect sites which enable an activating path for $H_2$ evolution, and no external chemical reduction with $H_2$ is required to introduce such defects.

**Charge Carrier Dynamics and Their Lifetimes.** Excitation−emission PL maps measured over a wide range of excitation wavelengths for $TiO_2$-BNS (Figure 6a) and $TiO_2$-BNS-$Pt_{0.05}$ (Figure 6b) help to understand charge carrier dynamics and their lifetimes within the active photocatalysts. For both samples, a similar PL emission was observed as follows: (i) PL emission at 392 nm corresponds to the band edge emission, whereas (ii) PL emission at 542 nm is related to oxygen vacancy defect states, that are generated due to the high surface energy of the large (010) surfaces of $TiO_2$-BNS.[42,43] $TiO_2$-BNS-$Pt_{0.05}$ shows a significant decrease in PL emission intensity at 542 nm, as compared to $TiO_2$-BNS which indicates that $TiO_2$-BNS-$Pt_{0.05}$ can effectively reduce the radiative recombination rate of photogenerated electron−hole pairs as photoexcited electrons preferred to migrate to Pt SAs, leading to improved separation of electron and hole pairs. Furthermore, the lifetimes of the charge carriers in both the samples were investigated by time-resolved photoluminescence (TRPL) measurements at both the emission wavelengths, i.e., 392 and 542 nm. As shown in Figure 6c, the corresponding PL lifetimes were obtained by fitting the data with a two-exponential decay functions as mentioned in the Experimental Section. The average PL lifetimes ($\tau_{ave}$) for $TiO_2$-BNS at 392 and 542 nm are 2.6 and 5.1 ns, respectively. However, the average PL lifetimes ($\tau_{ave}$) for the $TiO_2$-BNS-$Pt_{0.05}$ sample at 392 and 542 nm are 3.2 and 5.5 ns, respectively. The $\tau_{ave}$ values of the charge carriers in $TiO_2$-BNS-$Pt_{0.05}$ are higher than those retrieved for $TiO_2$-BNS in both the PL emission peaks, confirming the enhanced charge-separation efficiency and prolonged lifetimes of the excited electron−hole pairs once Pt SAs were anchored onto the $TiO_2$ surface,[24,44−46] thus

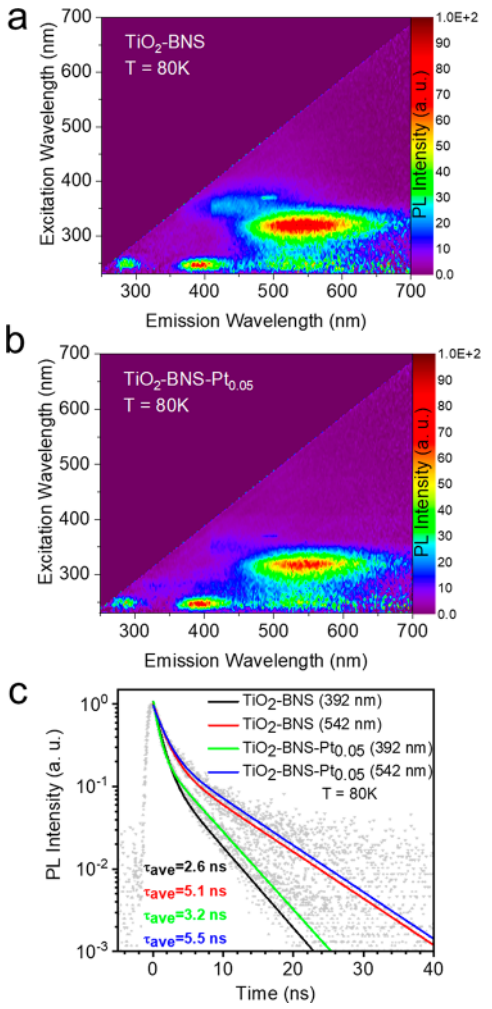


**Figure 6.** Photoexcited charge dynamics: Excitation–emission 2D color maps of (a) $TiO_2$-BNS and (b) $TiO_2$-BNS-$Pt_{0.05}$. (c) Time resolved PL spectra of $TiO_2$-BNS and $TiO_2$-BNS-$Pt_{0.05}$ samples collected at their corresponding PL maxima.

explaining the physical reason underlying the observed higher photocatalytic $H_2$ production rate for $TiO_2$-BNS-$Pt_{0.05}$ as compared to $TiO_2$-BNS. Thus, we have provided all the necessary figures of merit related to photocatalytic $H_2$ evolution reaction.[47]

## CONCLUSIONS

In summary, we presented the large-scale synthesis of ultrathin 2D $TiO_2$-bronze nanosheets ($TiO_2$-BNS) using an ethylene glycol solvothermal procedure under green mild conditions. Subsequent $H_2$ reduction generates black anatase $TiO_2$ nanosheets ($TiO_2$-HRNS). Both of these materials were investigated with advanced characterization methods and tested for photocatalytic $H_2$ evolution under both solar and UV light irradiation. Surprisingly, the reduced $TiO_2$-HRNS showed complete photo inactivity that was justified using FTIR, Raman, XPS, and EPR spectroscopy analyses. On the other hand, light-induced surface-exposed *in situ* $Ti^{3+}$ defect site generation in $TiO_2$-BNS was demonstrated to be responsible for significant $H_2$ production activity. Furthermore, an easy and scalable synthetic procedure was developed to decorate $TiO_2$-BNS with Pt SAs with very low loading, i.e., 0.05 wt %. $TiO_2$-BNS-$Pt_{0.05}$ shows efficient production of $H_2$ as compared to $TiO_2$-BNS, around 10 and 99 times higher rates under solar and 365 nm UV-LED light irradiation, respectively. These results demonstrate the potential of bronze $TiO_2$ nanosheets as efficient two-dimensional photocatalysts with high surface areas that are robust and cheap. This work highlights further that widely dispersed, strongly surface coordinated Pt SAs are the key to achieve high activities of photocatalytic systems with maximized $H_2$ production at minimum Pt loadings the cost of production. The strong interactions between Pt SAs with $TiO_2$-BNS provide channels to promote electron transfers to Pt SAs, thus prolonging photogenerated charge carrier lifetimes and resulting in enhanced photocatalytic $H_2$ production.

## AUTHOR INFORMATION


### Corresponding Authors

**Sourav Rej** – *Czech Advanced Technology and Research Institute, Regional Centre of Advanced Technologies and Materials, Palacký University Olomouc, 78371 Olomouc, Czech Republic*; Email: sourav.rej@upol.cz

**Alberto Naldoni** – *Czech Advanced Technology and Research Institute, Regional Centre of Advanced Technologies and Materials, Palacký University Olomouc, 78371 Olomouc, Czech Republic; Department of Chemistry and NIS Centre, University of Turin, 10125 Turin, Italy*; orcid.org/0000-0001-5932-2125; Email: alberto.naldoni@unito.it

### Authors

**S. M. Hossein Hejazi** – *Czech Advanced Technology and Research Institute, Regional Centre of Advanced Technologies and Materials, Palacký University Olomouc, 78371 Olomouc, Czech Republic; CEET, Nanotechnology Centre, VŠB-Technical University of Ostrava, 70800 Ostrava-Poruba, Czech Republic*

**Zdeněk Badura** – *Czech Advanced Technology and Research Institute, Regional Centre of Advanced Technologies and Materials, Palacký University Olomouc, 78371 Olomouc, Czech Republic*

**Giorgio Zoppellaro** – *Czech Advanced Technology and Research Institute, Regional Centre of Advanced Technologies and Materials, Palacký University Olomouc, 78371 Olomouc, Czech Republic*

**Sergii Kalytchuk** – *Czech Advanced Technology and Research Institute, Regional Centre of Advanced Technologies and Materials, Palacký University Olomouc, 78371 Olomouc, Czech Republic*; orcid.org/0000-0002-6371-8795

**Štěpán Kment** – *Czech Advanced Technology and Research Institute, Regional Centre of Advanced Technologies and Materials, Palacký University Olomouc, 78371 Olomouc, Czech Republic; CEET, Nanotechnology Centre, VŠB-Technical University of Ostrava, 70800 Ostrava-Poruba, Czech Republic*; orcid.org/0000-0002-6381-5093

**Paolo Fornasiero** − *Department of Chemical and Pharmaceutical Sciences, ICCOM-CNR Trieste Research Unit, INSTM-Trieste, University of Trieste, 34127 Trieste, Italy;* orcid.org/0000-0003-1082-9157

### Notes

The authors declare no competing financial interest.

## ■ ACKNOWLEDGMENTS

We gratefully acknowledge the financial support from the Operational Programme Research, Development and Education - European Regional Development Fund, project no. CZ.02.1.01/0.0/0.0/15_003/0000416 of the Ministry of Education, Youth and Sports of the Czech Republic. A.N. and S.R. acknowledge the support of the Czech Science Foundation (GACR) through the project no. 20-17636S.

## ■ REFERENCES

(1) Hisatomi, T.; Domen, K. Reaction Systems for Solar Hydrogen Production via Water Splitting with Particulate Semiconductor Photocatalysts. *Nat. Catal* **2019**, *2*, 387−399.
(2) Ahmad, H.; Kamarudin, S. K.; Minggu, L. J.; Kassim, M. Hydrogen from Photo-Catalytic Water Splitting Process: A Review. *Renewable and Sustainable Energy Rev.* **2015**, *43*, 599−610.
(3) Rej, S.; Bisetto, M.; Naldoni, A.; Fornasiero, P. Well-Defined $Cu_2O$ Photocatalysts for Solar Fuels and Chemicals. *J. Mater. Chem. A* **2021**, *9*, 5915−5951.
(4) Meng, A.; Zhang, L.; Cheng, B.; Yu, J. Dual Cocatalysts in $TiO_2$ Photocatalysis. *Adv. Mater.* **2019**, *31*, 1807660.
(5) Kumaravel, V.; Mathew, S.; Bartlett, J.; Pillai, S. C. Photocatalytic Hydrogen Production Using Metal Doped $TiO_2$: A Review of Recent Advances. *Appl. Catal., B* **2019**, *244*, 1021−1064.
(6) Naldoni, A.; Altomare, M.; Zoppellaro, G.; Liu, N.; Kment, S.; Zboril, R.; Schmuki, P. Photocatalysis with Reduced $TiO_2$: From Black $TiO_2$ to Cocatalyst-Free Hydrogen Production. *ACS Catal.* **2019**, *9*, 345−364.
(7) Zhang, J.; Zhou, P.; Liu, J.; Yu, J. New Understanding of the Difference of Photocatalytic Activity among Anatase, Rutile and Brookite $TiO_2$. *Phys. Chem. Chem. Phys.* **2014**, *16*, 20382−20386.
(8) Vequizo, J. J. M.; Matsunaga, H.; Ishiku, T.; Kamimura, S.; Ohno, T.; Yamakata, A. Trapping-Induced Enhancement of Photocatalytic Activity on Brookite $TiO_2$ Powders: Comparison with Anatase and Rutile $TiO_2$ Powders. *ACS Catal.* **2017**, *7*, 2644−2651.
(9) Dylla, A. G.; Stevenson, K. J. Electrochemical and Raman Spectroscopy Identification of Morphological and Phase Transformations in Nanostructured $TiO_2$ (B). *J. Mater. Chem. A* **2014**, *2*, 20331−20337.
(10) Etacheri, V.; Yourey, J. E.; Bartlett, B. M. Chemically Bonded $TiO_2$ − Bronze Nanosheet/Reduced Graphene Oxide Hybrid for High-Power Lithium Ion Batteries. *ACS Nano* **2014**, *8*, 1491−1499.
(11) Liang, S.; Wang, X.; Qi, R.; Cheng, Y.; Xia, Y.; Müller-Buschbaum, P.; Hu, X. Bronze-Phase $TiO_2$ as Anode Materials in Lithium and Sodium-Ion Batteries. *Adv. Funct. Mater.* **2022**, *32*, 2201675.
(12) Su, Q.; Li, Y.; Hu, R.; Song, F.; Liu, S.; Guo, C.; Zhu, S.; Liu, W.; Pan, J. Heterojunction Photocatalysts Based on 2D Materials: The Role of Configuration. *Adv. Sustainable Syst* **2020**, *4*, 2000130.
(13) Ayyub, M. M.; Singh, R.; Rao, C. N. R. Hydrogen Generation by Solar Water Splitting Using 2D Nanomaterials. *Sol. RRL* **2020**, *4*, 2000050.
(14) Ai, M.; Zhang, J.; Wu, Y.; Pan, L.; Shi, C.; Zou, J. Role of Vacancies in Photocatalysis: A Review of Recent Progress. *Chem. Asian J.* **2020**, *15*, 3599−3619.
(15) Qin, R.; Liu, P.; Fu, G.; Zheng, N. Strategies for Stabilizing Atomically Dispersed Metal Catalysts. *Small Methods* **2018**, *2*, 1700286.
(16) Li, Z.; Ji, S.; Liu, Y.; Cao, X.; Tian, S.; Chen, Y.; Niu, Z.; Li, Y. Well-Defined Materials for Heterogeneous Catalysis: From Nanoparticles to Isolated Single-Atom Sites. *Chem. Rev.* **2020**, *120*, 623−682.
(17) Gao, C.; Low, J.; Long, R.; Kong, T.; Zhu, J.; Xiong, Y. Heterogeneous Single-Atom Photocatalysts: Fundamentals and Applications. *Chem. Rev.* **2020**, *120*, 12175−12216.
(18) Qin, S.; Denisov, N.; Will, J.; Kolařík, J.; Spiecker, E.; Schmuki, P. A Few Pt Single Atoms Are Responsible for the Overall Co-Catalytic Activity in Pt/$TiO_2$ Photocatalytic $H_2$ Generation. *Sol. RRL* **2022**, *6*, 2101026.
(19) Hejazi, S.; Mohajernia, S.; Osuagwu, B.; Zoppellaro, G.; Andryskova, P.; Tomanec, O.; Kment, S.; Zbořil, R.; Schmuki, P. On the Controlled Loading of Single Platinum Atoms as a Co-Catalyst on $TiO_2$ Anatase for Optimized Photocatalytic $H_2$ Generation. *Adv. Mater.* **2020**, *32*, 1908505.
(20) Qin, S.; Denisov, N.; Sarma, B. B.; Hwang, I.; Doronkin, D. E.; Tomanec, O.; Kment, S.; Schmuki, P. Pt Single Atoms on $TiO_2$ Polymorphs—Minimum Loading with a Maximized Photocatalytic Efficiency. *Adv. Mater. Interfaces* **2022**, *9*, 2200808.
(21) Xiang, G.; Li, T.; Zhuang, J.; Wang, X. Large-Scale Synthesis of Metastable $TiO_2$ (B) Nanosheets with Atomic Thickness and Their Photocatalytic Properties. *Chem. Commun.* **2010**, *46*, 6801.
(22) Xiang, G.; Wang, Y.-G.; Li, J.; Zhuang, J.; Wang, X. Surface-Specific Interaction by Structure-Match Confined Pure High-Energy Facet of Unstable $TiO_2$ (B) Polymorph. *Sci. Rep* **2013**, *3*, 1411.
(23) Kang, J.; Zhang, Y.; Chai, Z.; Qiu, X.; Cao, X.; Zhang, P.; Teobaldi, G.; Liu, L.; Guo, L. Amorphous Domains in Black Titanium Dioxide. *Adv. Mater.* **2021**, *33*, 2100407.
(24) Wu, X.; Zhang, Q.; Li, W.; Qiao, B.; Ma, D.; Wang, S. L. Atomic-Scale Pd on 2D Titania Sheets for Selective Oxidation of Methane to Methanol. *ACS Catal.* **2021**, *11*, 14038−14046.
(25) Luo, X.; Ke, Y.; Yu, L.; Wang, Y.; Homewood, K. P.; Chen, X.; Gao, Y. Tandem CdS/$TiO_2$(B) Nanosheet Photocatalysts for Enhanced $H_2$ Evolution. *Appl. Surf. Sci.* **2020**, *515*, 145970.
(26) Xiang, G.; Tang, Y.; Liu, Z.; Zhu, W.; Liu, H.; Wang, J.; Zhong, G.; Li, J.; Wang, X. Probing Ligand-Induced Cooperative Orbital Redistribution That Dominates Nanoscale Molecule−Surface Interactions with One-Unit-Thin $TiO_2$ Nanosheets. *Nano Lett.* **2018**, *18*, 7809−7815.
(27) Hejazi, S. M. H.; Shahrezaei, M.; Błonski, P.; Allieta, M.; Sheverdyaeva, P. M.; Moras, P.; Badura, Z.; Kalytchuk, S.; Mohammadi, E.; Zboril, R.; Kment, S.; Otyepka, M.; Naldoni, A.; Fornasiero, P. Defect Engineering over Anisotropic Brookite toward Substrate-Specific Photo-Oxidation of Alcohols. *Chem. Catalysis* **2022**, *2*, 1177−1190.
(28) Naldoni, A.; Allieta, M.; Santangelo, S.; Marelli, M.; Fabbri, F.; Cappelli, S.; Bianchi, C. L.; Psaro, R.; Dal Santo, V. Effect of Nature and Location of Defects on Bandgap Narrowing in Black $TiO_2$ Nanoparticles. *J. Am. Chem. Soc.* **2012**, *134*, 7600−7603.
(29) Guo, W.; Zou, J.; Guo, B.; Xiong, J.; Liu, C.; Xie, Z.; Wu, L. Pd Nanoclusters/$TiO_2$ (B) Nanosheets with Surface Defects toward Rapid Photocatalytic Dehalogenation of Polyhalogenated Biphenyls under Visible Light. *Appl. Catal., B* **2020**, *277*, 119255.
(30) Liu, P.; Zhao, Y.; Qin, R.; Mo, S.; Chen, G.; Gu, L.; Chevrier, D. M.; Zhang, P.; Guo, Q.; Zang, D.; Wu, B.; Fu, G.; Zheng, N. Photochemical Route for Synthesizing Atomically Dispersed Palladium Catalysts. *Science* **2016**, *352*, 797−800.
(31) Wang, J.; Jia, H.; Guo, Y.; Zhang, Y.; Xie, Q.; Zhu, H.; Sun, J.; Shi, F.; Liu, Z.-H.; Jiang, R. ($TiO_2$ (B) Nanosheet)/(Metallic Phase $MoS_2$) Hybrid Nanostructures: An Efficient Catalyst for Photocatalytic Hydrogen Evolution. *Sol. RRL* **2019**, *3*, 1900323.
(32) Kaniyoor, A.; Ramaprabhu, S. A Raman Spectroscopic Investigation of Graphite Oxide Derived Graphene. *AIP Adv.* **2012**, *2*, 032183.

(33) Pan, D.; Jiao, J.; Li, Z.; Guo, Y.; Feng, C.; Liu, Y.; Wang, L.; Wu, M. Efficient Separation of Electron-Hole Pairs in Graphene Quantum Dots by $TiO_2$ Heterojunctions for Dye Degradation. *ACS Sustainable Chem. Eng.* **2015**, *3*, 2405−2413.
(34) Dong, Y.; Luo, X.; Wang, Y.; Ji, P.; Hong, X.; Wang, S.; Zhou, W.; Li, R.; Homewood, K. P.; Lourenco, M.; Gao, Y.; Chen, X. A Robust Novel 0D/2D $MoS_3$ QDs/C-Doped Atomically Thin $TiO_2$(B) Nanosheet Composite for Highly Efficient Photocatalytic $H_2$ Evolution. *Appl. Surf. Sci.* **2022**, *599*, 153972.
(35) Hang, Y. L.; Xing, J.; Jia, Z. C.; Li, Z.; Tian, F.; Zheng, L. R.; Wang, H. F.; Hu, P.; Zhao, H. j.; Yang, H. G. Unidirectional Suppression of Hydrogen Oxidation on Oxidized Platinum Clusters. *Nat. Commun.* **2013**, *4*, 2500.
(36) Lee, B.-H.; Park, S.; Kim, M.; Sinha, A. K.; Lee, S. C.; Jung, E.; Chang, W. J.; Lee, K.-S.; Kim, J. H.; Cho, S.-P.; Kim, H.; Nam, K. T.; Hyeon, T. Reversible and Cooperative Photoactivation of Single-Atom Cu/$TiO_2$ Photocatalysts. *Nat. Mater.* **2019**, *18*, 620−626.
(37) Wierzbicka, E.; Zhou, X.; Denisov, N.; Yoo, J.; Fehn, D.; Liu, N.; Meyer, K.; Schmuki, P. Self-Enhancing $H_2$ Evolution from $TiO_2$ Nanostructures under Illumination. *ChemSusChem* **2019**, *12*, 1900−1905.
(38) Doustkhah, E.; Assadi, M. H. N.; Komaguchi, K.; Tsunoji, N.; Esmat, M.; Fukata, N.; Tomita, O.; Abe, R.; Ohtani, B.; Ide, Y. In Situ Blue Titania via Band Shape Engineering for Exceptional Solar $H_2$ Production in Rutile $TiO_2$. *Appl. Catal., B* **2021**, *297*, 120380.
(39) Ji, Y.; Guo, W.; Chen, H.; Zhang, L.; Chen, S.; Hua, M.; Long, Y.; Chen, Z. Surface $Ti^{3+}/Ti^{4+}$ Redox Shuttle Enhancing Photocatalytic $H_2$ Production in Ultrathin $TiO_2$ Nanosheets/CdSe Quantum Dots. *J. Phys. Chem. C* **2015**, *119*, 27053−27059.
(40) Livraghi, S.; Chiesa, M.; Paganini, M. C.; Giamello, E. On the Nature of Reduced States in Titanium Dioxide As Monitored by Electron Paramagnetic Resonance. I: The Anatase Case. *J. Phys. Chem. C* **2011**, *115*, 25413−25421.
(41) Augustyniak-Jabłokow, M. A.; Strzelczyk, R.; Fedaruk, R. Localization of Conduction Electrons in Hydrothermally Reduced Graphene Oxide: Electron Paramagnetic Resonance Studies. *Carbon* **2020**, *168*, 665−672.
(42) Choudhury, B.; Bayan, S.; Choudhury, A.; Chakraborty, P. Narrowing of Band Gap and Effective Charge Carrier Separation in Oxygen Deficient $TiO_2$ Nanotubes with Improved Visible Light Photocatalytic Activity. *J. Colloid Interface Sci.* **2016**, *465*, 1−10.
(43) Makal, P.; Das, D. Superior Photocatalytic Dye Degradation under Visible Light by Reduced Graphene Oxide Laminated $TiO_2$-B Nanowire Composite. *J. Environ. Chem. Eng.* **2019**, *7*, 103358.
(44) Li, J.; Yi, D.; Zhan, F.; Zhou, B.; Gao, D.; Guo, D.; Liu, S.; Wang, X.; Yao, J. Monolayered $Ru_1/TiO_2$ Nanosheet Enables Efficient Visible-Light-Driven Hydrogen Evolution. *Appl. Catal., B* **2020**, *271*, 118925.
(45) Gao, C.; Wei, T.; Zhang, Y.; Song, X.; Huan, Y.; Liu, H.; Zhao, M.; Yu, J.; Chen, X. A Photoresponsive Rutile $TiO_2$ Heterojunction with Enhanced Electron-Hole Separation for High-Performance Hydrogen Evolution. *Adv. Mater.* **2019**, *31*, 1806596.
(46) Zhao, Y.; Zhao, Y.; Shi, R.; Wang, B.; Waterhouse, G. I. N.; Wu, L. Z.; Tung, C. H.; Zhang, T. Tuning Oxygen Vacancies in Ultrathin $TiO_2$ Nanosheets to Boost Photocatalytic Nitrogen Fixation up to 700 nm. *Adv. Mater.* **2019**, *31*, 1806482.
(47) Rej, S.; Santiago, E. Y.; Baturina, O.; Zhang, Y.; Burger, S.; Kment, Š.; Govorov, A. O.; Naldoni, A. Colloidal Titanium Nitride Nanobars for Broadband Inexpensive Plasmonics and Photochemistry from Visible to Mid-IR Wavelengths. *Nano Energy* **2022**, *104*, 107989.